COMPUTATIONAL FLUID DYNAMICS STUDY OF AN MPD THRUSTER

HIROYUKI YAMADA and TOSHI FUJIWARA

Depertment of Aeronautical Engineering

(Received October 31, 1986)

Abstract

A nonsteady two-dimensional analysis of an MPD accelerator is performed, taking Hall effect into consideration. Starting from a purely gasdynamical flow, the MHD equations are numerically integrated both inside and outside of the thruster using Argon as propellant. The calculated flow properties, e.g. current distribution, specific inpulse and thrust, agree well with available experimental observations.

1. Introduction

Magneto-plasmadynamic (MPD) thrusters realizing high specific impulse are good candidates among propulsion devices for orbital transportation of large space systems and interplanetary missions. Various versions of MPD thruster are developed for practical use, where detailed experiments have been performed and directed toward understanding the phenomena occurring inside the discharge chamber.

Regarding the associated numerical simulations, macroscopic behaviors of a plasma gas have been analyzed for the understanding of magneto-hydrodynamic phenomena in a thruster. Most of these analyses were quasi-one-dimensional steady-state ones, while exceptionally few were two-dimensional nonsteady (Refs. 1~3). Motivated by such situations, in the present study, we performed a nonsteady numerical simulation of magneto-hydrodynamic 2-D flows based on the one-fluid model, in an attempt to compare with existing experiments.

The difference scheme utilized to solve the MHD equations is the second-order-accurate explicit MacCormack-FCT method. The calculated domain is extended outside the thruster in comparison with the previous analysis (Ref. 1). It

should be noted here that the fundamental equations consist of both 1st- and 2nd-order partial differential terms; this causes a problem in the choice of integration time increment. In order to overcome the difficulty, the SOSA method regarding how to solve mixed-order equations is proposed and found out effective. The details are described in Section 3.

2. Formulation of the Ploblem

1) Assumptions

The following assumptions have been made in a series of magneto-hydrodynamic analyses conducted so far by our group (Refs. 1~3):

(1) The collision frequency of plasma particles is high enough to establish local thermodynamic equilibrium. Thus, ĵhe plasma gas in the thruster can be considered a continuum fluid, that holds macroscopic electrical neutrality and is fully ionized. Although the plasma is composed of electrons and ions in reality (two-component model), its fundamental properties can be described by local macroscopic mean values (single-component model). Therefore, no microscopic phenomena, e. g. the electrode sheath or propellant starvation, can be handled. In addition, the plasma gas obeys the perfect-gas equation of state

(2) No ionization processes, chemical reactions, heat of reaction and transport phenomena other than electric and magnetic conductions are considered. Thus the plasma gas is ionized already at the inlet of a thruster, which constitutes the upstream boundary of the flow field.

(3) The thruster geometry and employed cylindrical coordinate system are shown in Fig. 1. The thruster is composed of a hollow cylindrical anode and a cone-cylinder-shaped cathode, corresponding to the experimental device of our group. Thus the axisymmetric gasdynamic and electromagnetic fields are considered.

(4) The existing magnetic field is entirely self-induced, having the azimuthal component only. The generalized Ohm law holds between the electic field and current density, taking account of the Hall effect. Ion slip effect and electron pressure, the terms based on a two-component model, are not considered. In this study, the plasma is assumed isotropic whether the Larmor radius of electron is longer than mean free path or not. Thus the electric conductivity is a scalar value given by the Spitzer-Härm formula. The displacement current term in the Maxwell equation is neglected because it is considered that the propagation speed of perturbation is much less than that of light.

(5) The velocity, pressure and mass flow rate at the inlet, and the total discharge current are the specified quantities. Argon is utilized as propellant.

2) Magneto-Hydrodynamical Equations

The fundamental equations governing plasma gas motion are written as follows:

Continuity $\dfrac{\partial \rho}{\partial t} + \mathrm{div}\,(\rho\boldsymbol{V}) = 0,$ (1)

Momentum $\rho\dfrac{D\boldsymbol{V}}{Dt} = -\mathrm{grad}\,p + \boldsymbol{j}\times\boldsymbol{B},$ (2)

Energy
$$\frac{\partial}{\partial t}(q+\frac{|\boldsymbol{B}|^2}{2\mu_0})+\mathrm{div}((q+p)\,\boldsymbol{V}+\frac{\boldsymbol{E}\times\boldsymbol{B}}{\mu_0})=0, \tag{3}$$

$$q=\frac{1}{2}\rho|\boldsymbol{V}|^2+\frac{1}{\gamma-1}\rho RT, \tag{4}$$

State
$$p=\rho RT, \tag{5}$$

Maxwell
$$\frac{\partial \boldsymbol{B}}{\partial t}=-\mathrm{rot}\,\boldsymbol{E}, \tag{6}$$

$$\boldsymbol{j}=\frac{1}{\mu_0}\mathrm{rot}\,\boldsymbol{B}, \tag{7}$$

Ohm law
$$\boldsymbol{j}=\sigma(\boldsymbol{E}+\boldsymbol{V}\times\boldsymbol{B})-\mu_e(\boldsymbol{j}\times\boldsymbol{B}). \tag{8}$$

The variables ρ, $\boldsymbol{V}$, p, T, $\boldsymbol{B}$, $\boldsymbol{j}$ and $\boldsymbol{E}$ denote the plasma mass density, velocity, pressure, temperature, magnetic flux density, current and electric field. R is the gas constant, μ_0 the magnetic permeability of vacuum and γ the specific heat ratio. σ and μ_e in the Ohm law signify the electric conductivity and mobility, where the conductivity treated as a scalar in this study, can be expressed as follows using the Spitzer-Härm formula for a Lorentz gas that is a fully ionized plasma (Ref. 4):

$$\sigma=\left[\frac{2kT}{\pi}\right]^{3/2}m_e^{-1/2}e^{-2}(\ln\Lambda)^{-1}=f(T^{3/2},\ \Lambda), \tag{9}$$

$$\Lambda=\frac{3}{2e^2}\left[\frac{2(4\pi\varepsilon_0 kT)^3}{\pi n_i}\right]^{1/2}=g(T^{3/2},\ \rho^{1/2}), \tag{10}$$

$$n_i=n_e=\rho/m_i, \tag{11}$$

where k, e, ε_0, m_e, m_i, n_e and n_i are the Boltzman constant, the electricity quantum, the electric permittivity of vacuum, the electron mass, the ion mass, the number densities of electron and ion, respectively. There is an important relation between the conductivity and mobility, written as follows:

$$\mu_e=\sigma/(en_e). \tag{12}$$

Using this relation, the magneto-hydrodynamic equations become a closed system. The situation may be further simplified by eliminating the valiables $\boldsymbol{E}$ and $\boldsymbol{j}$. This is done by solving Eq. (8) with respect to $\boldsymbol{E}$:

$$\boldsymbol{E}=\sigma^{-1}(\boldsymbol{j}+\mu_e\boldsymbol{j}\times\boldsymbol{B})-\boldsymbol{V}\times\boldsymbol{B}. \tag{13}$$

Substitution of $\boldsymbol{j}$ from Eq. (7) gives

$$\frac{\partial \boldsymbol{B}}{\partial t}=\mathrm{rot}[\boldsymbol{V}\times\boldsymbol{B}-\frac{1}{\sigma\mu_0}(\mathrm{rot}\,\boldsymbol{B}+\mu_e(\mathrm{rot}\,\boldsymbol{B})\times\boldsymbol{B})] \tag{14}$$

which is the equation of induction. Since the Spitzer-Härm formula (9) gives the electric conductivity σ as a function of plasma density and temperature, where the transport property is assumed constant, Eq. (14) becomes similar to the Navier-

Stokes equation. Clearly the reciprocal of conductivity plays a role of kinematic viscosity.

The physical properties are non-dimensionalized as in the following:

$$\left.\begin{array}{l} \rho=\dfrac{\dot{m}}{V_m}\hat{\rho}, \quad V=V_m\hat{V}, \quad T=\dfrac{V_m^2}{R}\hat{T}, \quad P=P_m\hat{P}, \\[3mm] \boldsymbol{B}=B_0\hat{\boldsymbol{B}}, \quad \boldsymbol{E}=V_mB_0\hat{\boldsymbol{E}}, \quad \boldsymbol{j}=\dfrac{B_0}{2\mu_0R_c}\hat{\boldsymbol{j}}, \quad \sigma=\sigma_0\hat{\sigma}, \\[3mm] r, \ z=R_c\cdot\hat{r}, \ \hat{z}, \quad t=\dfrac{R_c}{V_m}\hat{t}, \\[3mm] B_0=\dfrac{\mu_0J}{2\pi R_c}, \quad P_m=\dfrac{B_0^2}{2\mu_0}, \quad V_m=\dfrac{B_0^2}{2\mu_0\dot{m}}, \quad J=\int j\cdot ds, \end{array}\right\} \tag{15}$$

where R_c represents the cathode radius, V_m and P_m the magnetic acoustic speed and the magnetic pressure at the inlet, $\dot{m}$ the mass flow rate per unit area, B_0 the magnetic flux density on the cathode root surface, σ_0 the conductivity at the inlet and J the total current, respectively.

Using the dimensionless variables, the fundamental equations in the cylindrical coordinate system can be written in the conservation form

$$\frac{\partial f}{\partial\hat{t}}+\frac{1}{\hat{r}}\frac{\partial}{\partial\hat{r}}(\hat{r}F)+\frac{\partial G}{\partial\hat{r}}+\frac{\partial H}{\partial\hat{z}}=0, \tag{16}$$

$$f=\begin{pmatrix}\hat{\rho}\\\hat{\rho}\hat{u}\\\hat{\rho}\hat{v}\\\hat{e}+\hat{B}^2\\\hat{B}\end{pmatrix}, \ F=\begin{pmatrix}\hat{\rho}\hat{u}\\\hat{\rho}\hat{u}^2+2\hat{B}^2\\\hat{\rho}\hat{u}\hat{v}\\(\hat{e}+\hat{\rho}\hat{T})\hat{u}\\0\end{pmatrix}, \ G=\begin{pmatrix}0\\\hat{\rho}\hat{T}-\hat{B}^2\\0\\-2\hat{B}\hat{E}_z\\-\hat{E}_z\end{pmatrix}, \ H=\begin{pmatrix}\hat{\rho}\hat{u}\\\hat{\rho}\hat{u}\hat{v}\\\hat{\rho}\hat{v}^2+\hat{\rho}\hat{T}+\hat{B}^2\\(\hat{e}+\hat{\rho}\hat{T})\hat{v}+2\hat{B}\hat{E}_r\\\hat{E}_r\end{pmatrix},$$

$$\hat{e}=\frac{1}{2}\hat{\rho}(\hat{u}^2+\hat{v}^2)+\frac{1}{\gamma-1}\hat{\rho}\hat{T},$$

$$\begin{pmatrix}\hat{E}_r\\\hat{E}_z\end{pmatrix}=\begin{pmatrix}\hat{v}\hat{B}\\-\hat{u}\hat{B}\end{pmatrix}+\frac{1}{2R_m\hat{\sigma}}\begin{pmatrix}1 & -h_e\hat{B}\\h_e\hat{B} & 1\end{pmatrix}\begin{pmatrix}-2\dfrac{\partial\hat{B}}{\partial\hat{z}}\\[3mm]\dfrac{2}{\hat{r}}\dfrac{\partial}{\partial\hat{r}}(\hat{r}\hat{B})\end{pmatrix},$$

$$h_e=\mu_eB=\frac{m_i}{e}\left(\frac{B\sigma}{\rho}\right), \quad R_m=\mu_0\sigma_0V_mR_c, \tag{17}$$

$$\hat{\boldsymbol{V}}=(\hat{V}_r, \ \hat{V}_\theta, \ \hat{V}_z)=(\hat{u}, \ 0, \ \hat{v}), \quad \hat{\boldsymbol{B}}=(0, \ \hat{B}, \ 0), \quad \hat{\boldsymbol{E}}=(\hat{E}_r, \ 0, \ \hat{E}_z),$$

where R_m and h_e are called the magnetic Reynolds number and Hall parameter.

3. Method of Analysis

1) *Explicit MacCormack-FCT Difference Scheme*

The utilized finite difference scheme is the 2 nd-order explicit MacCormack method, where the FCT smoothing technique is added to ensure the stability of the solution. The dimensionless fundamental equations (16) in a conservation form can be factorized into the following two one-dimensional equations in r and z directions using the time-splitting technique :

$$\frac{\partial f}{\partial t}+\frac{1}{r}\frac{\partial}{\partial r}(rF)+\frac{\partial G}{\partial r}=0, \quad (18)$$

and
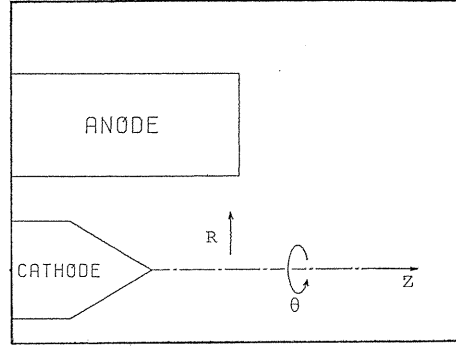
Fig. 1. Thruster geometry and coordinate system.

$$\frac{\partial f}{\partial t}+\frac{\partial H}{\partial z}=0. \quad (19)$$

To the one-dimensional equations in r direction (18), the 2nd-order MacCormack-FCT scheme is applied as follows :
(1) MacCormack Method :

$$\text{Predictor}\;;\; f_i^*=f_i^n-\frac{\Delta t}{r_i\Delta r}(r_iF_{i+1}^n-r_{i-1}F_i^n)-\frac{\Delta t}{\Delta r}(G_{i+1}^n-G_i^n), \quad (20)$$

$$\text{Corrector}\;;\; \hat{f}_i^{n+1}=\frac{1}{2}[f_i^n+f_i^*-\frac{\Delta t}{r_i\Delta r}(r_{i+1}F_i^*-r_iF_{i-1}^*)-\frac{\Delta t}{\Delta r}(G_i^*-G_{i-1}^*). \quad (21)$$

(2) FCT Technique :

$$\text{Diffusion}\;;\; \overline{f}_i^{n+1}=\hat{f}_i^{n+1}+\eta[\frac{r_{i+1/2}}{r_i}(f_{i+1}^n-f_i^n)-\frac{r_{i-1/2}}{r_i}(f_i^n-f_{i-1}^n)], \quad (22)$$

$$\text{Anti-diffusion}\;;\; f_i^{n+1}=\overline{f}_i^{n+1}+\frac{r_{i-1/2}}{r_i}\delta_{i-1/2}^c-\frac{r_{i+1/2}}{r_i}\delta_{i+1/2}^c, \quad (23)$$

where

$$r_{i+1/2}=(r_i+r_{i+1})/2, \quad (24)$$

$$\delta_{i+1/2}^c=S\cdot\max[0,\;\min\{S\cdot\frac{r_i}{r_{i+1/2}}\Delta_{i-1/2},\;|\overline{\Delta}_{i+1/2}|,\;S\cdot\frac{r_{i+1}}{r_{i+1/2}}\Delta_{i+3/2}\}], \quad (25)$$

$$\Delta_{i+1/2}=\overline{f}_{i+1}^{n+1}-\overline{f}_i^{n+1}, \quad (26)$$

$$\overline{\Delta}_{i+1/2}=\eta(\hat{f}_{i+1}^{n+1}-\hat{f}_i^{n+1}), \quad (27)$$

$$S = \text{sign}(\bar{A}_{i+1/2}). \tag{28}$$

The superscript n denotes the time index and the subscript i the spatial one. η is an empirical constant, chosen currently as 1/8. The z-direction counterpart is obtained by setting $\Delta r = \Delta z$ and $r = 1$ in Eqs. (20)~(28).

The time-advancing operator $L(\Delta t)$ can be approximated within 2nd-order accuracy by the MacCormack-FCT difference operator $L_r(\Delta t)$ in r-direction and $L_z(\Delta t)$ in z-direction as follows:

$$f_i^{n+1} = L(\Delta t) f_i^n, \tag{29}$$

$$L(\Delta t) = L_z\left(\frac{\Delta t}{2}\right) L_r(\Delta t) L_z\left(\frac{\Delta t}{2}\right), \tag{30}$$

the details of which are shown in Ref. 5.

2) CFL Condition and SOSA Technique

The stability criteria for the following two model equations are

$$\frac{\partial f}{\partial t} = -c \frac{\partial f}{\partial x} \qquad\qquad \Delta t_1 \leq \left[\frac{|c|+a}{\Delta x}\right]^{-1}, \tag{31}$$

$$\frac{\partial f}{\partial t} = -c \frac{\partial f}{\partial x} + \nu \frac{\partial^2 f}{\partial x^2} \qquad \Delta t_2 \leq \left[\frac{|c|+a}{\Delta x} + \frac{2\nu}{\Delta x^2}\right]^{-1}, \tag{32}$$

where a is the magnetic acoustic speed, i.e. the phase velocity of Alfvén wave (Ref. 6):

$$a = \left[\frac{|B|^2}{\mu_0 \rho} + \gamma RT\right]^{1/2}, \tag{33}$$

If ν (equal to $1/\sigma\mu_0$) is very large, Eqs. (31) and (32) clearly show that Δt_2 becomes much shorter than Δt_1, forcing Δt_2 to be utilized to solve the entire equations. In this case, however, even if one uses the fastest computer, the physical time of the phenomenon is too long to be covered. On the other hand, the time advances by practical amount if we are able to employ Δt_1. Thus it was attempted to solve Eqs. (31) and (32) alternatively; first, pure gasdynamics was solved assuming the B-E field known. However, it turned out that this method was not flexible enough to allow significant changes in the magnetic and electric fields, causing ever-oscillatory numerical instabilities.

In order to avoid these difficulties, we advanced the time by using a technique which we call Switch-Over Successive Approximation (SOSA). This is described as follows: First, the computation is carried out for the full equations by several steps using a short time step Δt_2, and thereafter both magnetic and electric fields are treated frozen where the energy and induction equations are needless to solve. Since the remaining equations consist only of 1st-order differential terms, a much longer time step Δt_1 can be chosen. The SOSA method repeats these operations.

3) Boundary Conditions

In general, grid cells are specified as rectangles located in parallel with the axis of symmetry.

The boundary conditions on the solid surface are imposed as follows (Refs. 2~3) :

$$V_n = E_t = 0, \text{ and } \frac{\partial f}{\partial n} = 0 \; ; \; f = \rho, \; V_t, \; T, \; E_n \text{ and } B, \qquad (34)$$

where the subscripts n and t represent the components normal and tangential to the solid surface, respectively, and n the outward normal unit vector. Both over the horizontal surface of the anode and on the cylindrical part of the cathode, two grid points are symmetrically placed across the surface where the principle of reflection is applied. The conical part of the cathode is treated in a complicated manner. In other words, there is no symmetry, with respect to the boundary, between the two closest points across the surface. Therefore, the property at the inner point symmetrical to an outer grid point is calculated by simple interpolation. As to vector quantities like velocity and electric field, it may be more convenient to use a conventional rotational transformation.

The boundary conditions on the axis of symmetry are as follows :

$$At \; r = 0 \; ; \; u = E_r = B = 0 \text{ and } \frac{1}{r} \frac{\partial}{\partial r} (fr) = 0, \qquad (35)$$

where $f = \rho, \; v, \; T$ and E_z. Since the axis has singular characters, the grids are shifted by a half radial mesh size, and then the principle of reflection is applied.

At the inlet of the thruster, each property remains unchanged from its initial value.

At the free boundary outside the thruster, we use the extrapolation technique while setting the magnetic flux density zero.

In order for the propellant plasma to be regarded as an isotropic continuum gas in the present analysis, the Knudsen number must be much less than unity, i.e. the following relation must hold :

$$K_n = l/L \ll 1, \qquad (36)$$

where l is the mean free path and L a characteristic body dimension, typically the anode radius, and the mean free path is expressed as (Ref. 7) ;

$$l = \frac{1}{\sqrt{2} \pi d^2} \times \frac{1}{n}, \qquad (37)$$

where d and n are the diameter and number density of the gas molecule. In the present calculation, we set $L = 10$cm, $d = 10^{-8}$cm and $n = 10^{17}$ molecule/cm^3, and therefore $K_n = 2 \times 10^{-3} \ll 1$ holds with a safe margin.

4. Results and Discussions
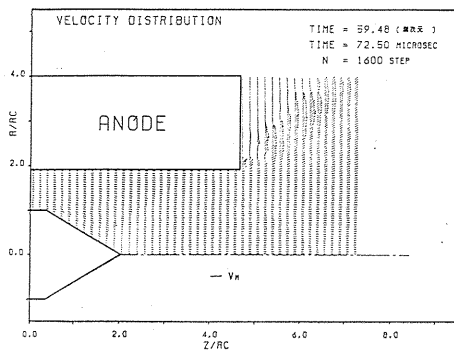
1) Purely Gasdynamic Flow

The values of the parameters utilized in this calculation are tabulated in Table 1, being selected in view of existing experiments. The parameter $J^2/\dot{m}$ appearing in the magnetic Reynolds number has a critical limit $(J^2/\dot{m})_{cr}$, above which

Table 1. The parameters utilized in the calculation.

Property	Inlet Condition (fixed at $z=0$)	Reference Value (at $r=r_c$, $z=0$)
Density	$\rho_{in}=1.0\times10^{-3}$ g/cm³	$\rho_m=0.22\times10^{-3}$ g/cm³
Velocity	$V_{in}=1300$ m/sec	$V_m=5904$ m/sec
Pressure	$P_{in}=575$ Pa ($\sim$4.3 torr)	$P_m=7680$ Pa ($\sim$57.6 torr)
Temperature	$T_{in}=2760$ K	$T_m=1.67\times10^5$ K
Magnetic flux density	$B_{in}=\dfrac{r_c}{r}B_m$ gauss	$B_m=1390$ gauss
Electric field	——	$E_m=8.20$ V/cm
Current density	——	$J_m=0.768$ kA/cm²
Characteristic length	——	$r_c=0.72$ cm (cathode radius)

Fixed properties at inlet		Geometry parameters	
Mass flow rate	$\dot{m}=0.553$ g/sec	L/r_c	4.667
Mach number	$M_{in}=1.3$	L_c/L	0.438
Magnetic Reynolds number	$(Re)_m=0.1188$	r_a/r_c	1.90
		Φ	62°
Total discharge current	$J=5$ kA	Rectanqular grid cell	
Parameter	$J^2/\dot{m}=45.2$ kA²/(g/sec)	$\Delta r\times\Delta z=0.050\times0.087$	

L ; Thruster length r_c ; Cathode radius
L_c ; Cathode length r_a ; Anode bore
                           Φ ; Cone angle of cathode tip
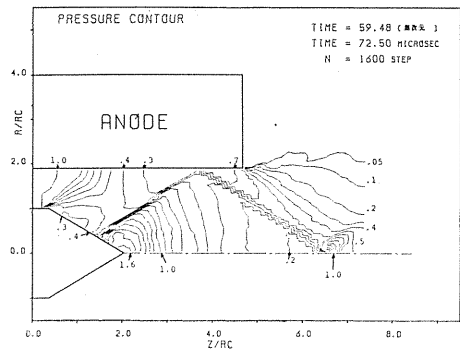
2 (a)   2 (b)

Fig. 2. (a) Steady velocity distribution and (b) pressure contours for a simple
    gasdynamic flow. The parameter on each contour is the pressure
    non-dimensionalized by the inlet value.

physical instabilities occur. In this study, this parameter is selected lower than the critical value 65. 4(kA^2/(g/sec)) for Argon propellant.

Figs. 2 (a) and 2 (b) show the velocity distribution and the pressure contour for a simple gasdynamic flow, which reaches a steady state at 72. 50 μsec (1400 time steps out of total 1600) after starting calculation. Expansion occurs at the cathode corner and interferes with a detached shock wave formed upstream of the cathode tip. The shock wave is incident on the anode wall and a reflected shock is formed. The calculated Mach angle 53 degree agrees reasonably well with the theoretical value 50. 3 degree corresponding to the incident Mach number $M=1.30$. Thus it is confirmed that the present numerical scheme can be properly applied to the next magneto-hydrodynamic problem.

2) Magneto-Hydrodynamic Flow without Hall Effect

As a technique to solve full MHD equations, the magneto-hydrodynamical effect is added to the steady-state purely-gasdynamic flow which is established in the previous section. The initial condition is naturally a current density distribution from physical point of view. However, it is more convenient to initially assume magnetic flux density because otherwise the magnetic field must be solved from the Maxwell equation (9). The assumed initial distribution of magnetic flux density is shown in Fig. 3 in the form of intensity contours, where the highest intensity is seen at the cathode root.

The SOSA method is applied after the entire equations have been solved using Δt_2 from 1601 to 2000 time steps to eliminate the influence of artificial initial distribution. The ratio between the step numbers in solving the full and hydrodynamic equations is chosen 3 to 1. In order to avoid numerical instabilities, the Hall effect is excluded until a nearly steady state is established.

The temporal behaviors of the magnetic flux density and velocity are shown in Figs. 4 and 5. The intensities of the magnetic field are higher in the vicinity of the cathode. Near the cathode surface, in particular, they are practically identical

Fig. 3. Initially assumed magnetic flux intensity distribution.

to the one at the cathode root. Thus the magnetic field abruptly changes at the cathode tip region because it must be zero on the axis. By 29200 time steps, the intensity contours ($\hat{B}>0.6$) distribute most densely along the cathode geometry and a high magnetic pressure field is formed. In this region, the distribution of B can be well approximated by the n-th power of $\hat{r}=r/R_c$:

$$\hat{B}(\hat{r}, \hat{z}) = A(\hat{z}) \cdot \hat{r}^{-n(z)}, \tag{38}$$

where $A(\hat{z})$ is a coefficient and $n(\hat{z})$ a power exponent, both of which are the functions of $\hat{z}=z/R_c$. As shown in Fig. 6 (a), $n(\hat{z})$ is nearly unity over the cylindrical part of the cathode ($\hat{z}<0.4$), while $n(\hat{z})$ begins to decrease linearly in the conical part ($0.4<\hat{z}<2.0$) as the discharge current flows into the cathode:
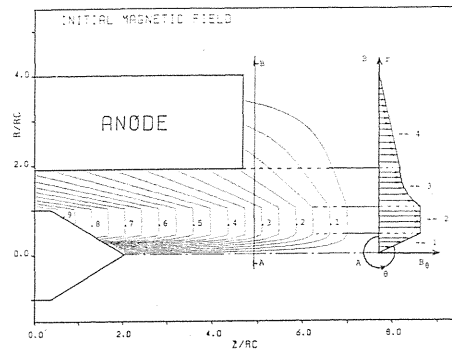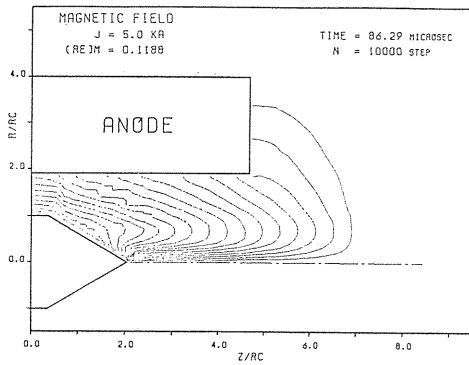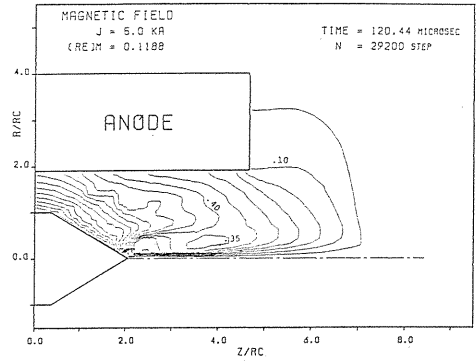
MAGNETIC FIELD
J = 5.0 KA
(RE)M = 0.1188
TIME = 86.29 MICROSEC
N = 10000 STEP

ANODE

4 (a)

MAGNETIC FIELD
J = 5.0 KA
(RE)M = 0.1188
TIME = 120.44 MICROSEC
N = 29200 STEP

ANODE

4 (c)

MAGNETIC FIELD
J = 5.0 KA
(RE)M = 0.1188
TIME = 103.10 MICROSEC
N = 19600 STEP

ANODE

4 (b)

Fig. 4. Temporal behaviors of magnetic flux intensity without Hall effect (R_m=0.1188).

$$n(\hat{z}) = -0.41\hat{z} + 1.13 \tag{39}$$

The correlation coefficient between the numerical results and Eq. (39) is more than 0.9, indicating that the curve is well fitted. The approximation does not hold in the region $\hat{z} > 2.0$ because of the singularity on the axis. The distribution of B in the axial direction is shown in Fig. 7, where the magnetic flux density decreases in proportion to $\hat{z}^{1.6}$ over the cathode-existing range $\hat{z} < 2.0$:

$$A(\hat{z}) = 1.0 - 0.23\hat{z}^{1.6} \tag{40}$$

Thereafter, it linearly decreases to the downstream boundary value. Hence the effect of the thruster geometry clearly appears.

As seen in Fig. 5, the plasma fluid is greatly accelerated inside the anode. As a result, the average exhaust velocity at the thruster exit reaches about 7 times as high as at the inlet, increasing Isp up to 1000 sec. The Lorentz force is primarily responsible for accelerating the propellant plasma toward the axial direction in the interelectrode region; however, acceleration also occurs in the radial direction after the plasma has spurted out from the thruster exit. Thus the plasma is accelerated to the direction perpendicular to both current-flow and azimuthally induced magnetic field.

VELOCITY DISTRIBUTION
J = 5.0 KA
(RE)M = 0.1188
TIME = 86.29 MICROSEC
N = 10000 STEP

ANODE

5(a)

VELOCITY DISTRIBUTION
J = 5.0 KA
(RE)M = 0.1188
TIME = 103.10 MICROSEC
N = 19600 STEP

ANODE

5(b)

VELOCITY DISTRIBUTION
J = 5.0 KA
(RE)M = 0.1188
TIME = 120.44 MICROSEC
N = 29200 STEP

ANODE

→ 5 × Vm

Z/RC
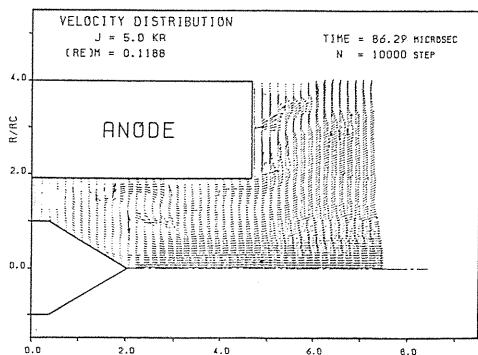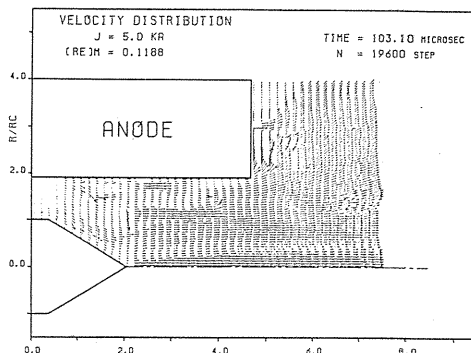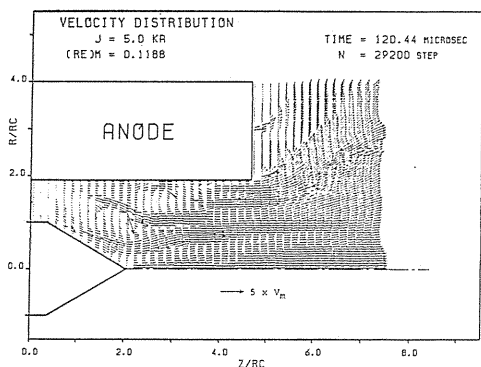
5(c)

Fig. 5. Temporal behaviors of velocity vectors without Hall effect ($R_m = 0.1188$).

The distribution of electric field vectors at 29200 time steps is shown in Fig. 8 (a). In contrast with the previous study yielding virtually radial components only, the present analysis gives rather smooth and reasonable distribution. The improvement is due to the correct treatment of magnetic field. Note that the electric field sandwiched between the cathode and anode is strong.

The current distribution at 29200 time steps is displayed in Fig. 8 (b), where the number on each contour indicates the current non-dimensionalized by the total discharge current. Interestingly, this current distribution is quite similar to the experimental results (Ref. 9), as shown in Fig. 9, even if the utilized parameters are different to some extent. The current distributions on the anode wall are nonuniform; in particular, the current concentrates on the anode rectangular corner, whereas it spreads on the inner anode surface. Inside the thruster, the current leaves anode surface radially, then flowing axially toward the conical part of the cathode. As the current flows nearly in the axial direction, the pumping force tends to accelerate the plasma rather than the blowing force does. This is proved by the plasma density and pressure, shown in Figs. 8 (c) and (d), high near the axis because of compression. The plasma density contours, shown in Fig. 8 (c), indicate that the plasma has not completely concentrated onto the axis. More results are yet to come.
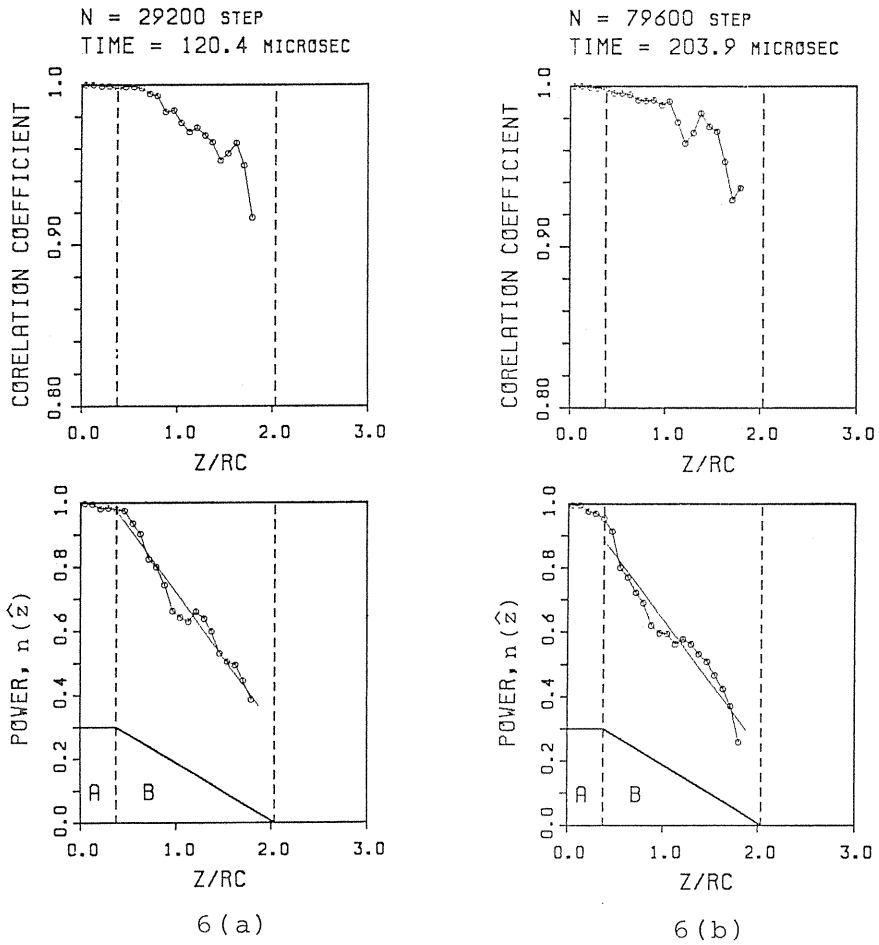
N = 29200 STEP
TIME = 120.4 MICROSEC

N = 79600 STEP
TIME = 203.9 MICROSEC

6 (a)

6 (b)

Fig. 6. Power and correlation coefficient profiles at (a) $t=120.4$ μsec and (b) $t=203.9$ μsec.
[A]: Cylindrical part of cathote.
[B]: Conical part of cathode.
The distribution of magnetic flux density is fitted into a curve that is a function of n-th power of r using regression analysis. The closer to unity the correlation coefficient is, the better the curve is fitted.

N = 29200 STEP
TIME = 120.4 MICROSEC
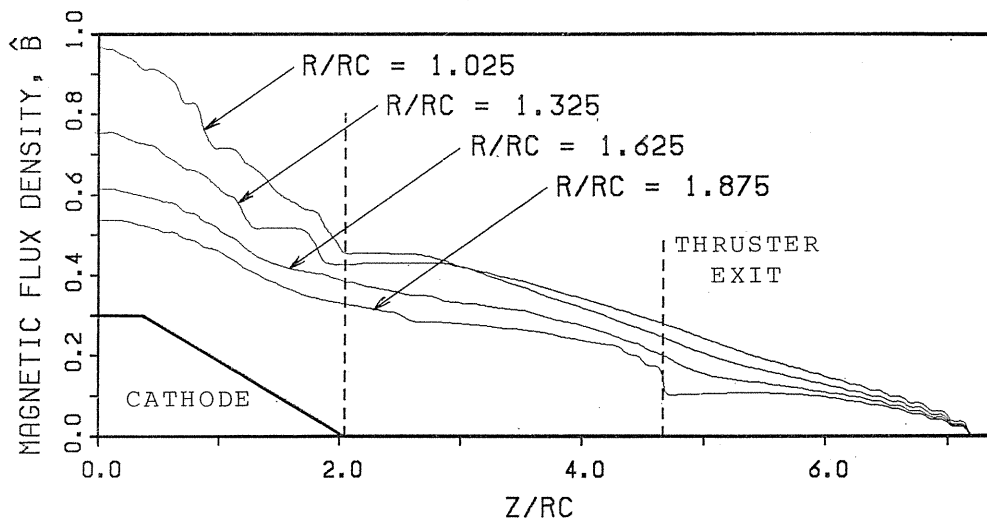
Fig. 7. Magnetic flux density profile in axial direction. The broken line at $r=4.667$ indicates the location of the thruster exit ($R_m=0.1188$).

8(a)

8(b)

8(c)

8(d)
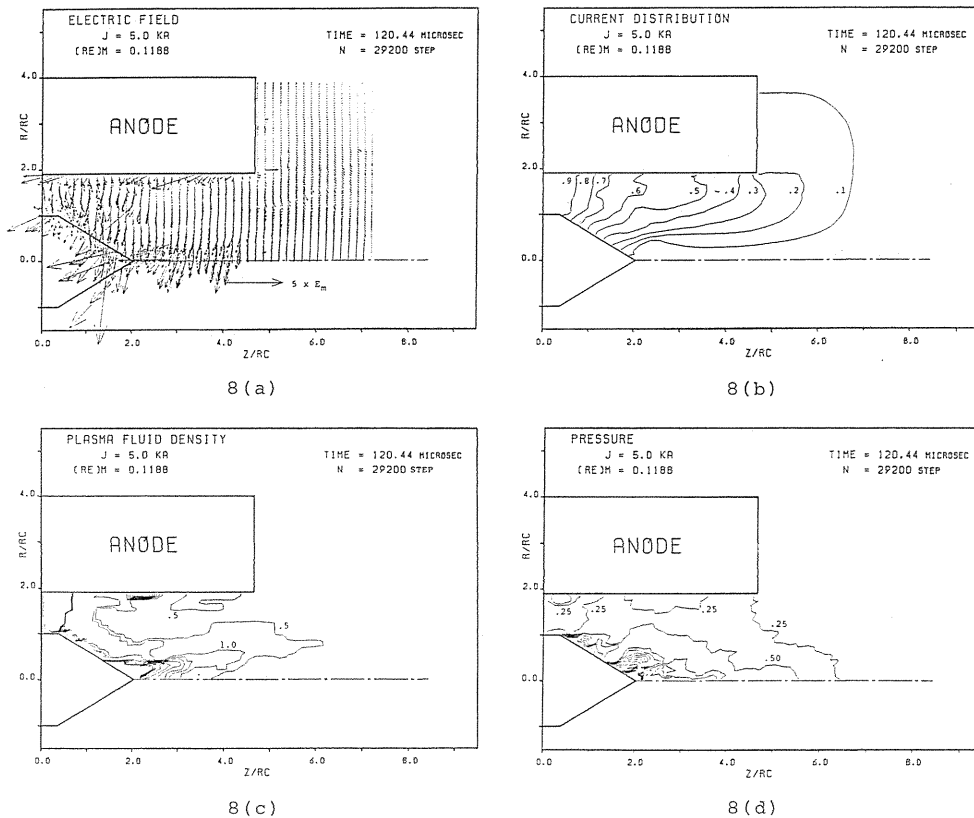
Fig. 8. (a) Electric field vector distribution, (b) current distribution contours, (c) plasma density contours and (d) pressure contours without Hall effect ($R_m=0.1188$).
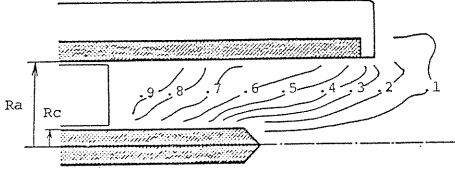
Fig. 9. Current distribution obtained from experiments (Ref. 9): Propellant Ar, Mass flow rate 0.62 g/sec, Discharge current 10.1 kA and R_a/R_c 5.26.

3) *Magneto-Hydrodynamic Flow with Hall Effect*

The temporal behaviors of magnetic field and velocity taking the Hall effect into account are shown in Figs. 10 and 11. Since the Hall current flows into the direction perpendicular to both magnetic flux density vector and effective electric field vector, it distorts the current to increase the axial component, as shown in Fig. 12(a). As a result, the magnetic field intensity in the axial direction holds a constant value 0.3~0.4 inside the thruster ($2.0 < \hat{z} < 4.0$), where a cylindrical plasma column seems to be formed. This can be readily seen in the plasma density distribution at 79600 time steps, shown in Fig. 12(b): The plasma density concentrates in the axial region and the pressure near the cathode tip is very high due to compression. Fig. 12(c) shows the pressure contours at 79600 time steps. We can conclude that the distribution of B in the upstream region $\hat{z} < 2.0$ is insensitive to the Hall effect, when we compare the two cases, with and without the Hall effect. When the distribution is reduced to the power law (38), the exponet $n(\hat{z})$ turns out to be slightly smaller, as shown in Fig. 6(b). At the downstream boundary, the boundary condition $\hat{B}=0$ is forced, preventing the magnetic field from propagating further downstream.

The total thrust F_t and specific inpulse Isp are obtained from the integration over the exit cross section:

$$F_t = \int_s \rho v^2 dS = 2\pi \int_{exit} \rho v^2 r dr, \tag{41}$$

$$I_{sp} = F_t / \left[g \cdot 2\pi \int_{exit} \rho v r dr \right]. \tag{42}$$

The temporal variations of the thrust and Isp are shown in Fig. 13. After the Isp has rapidly increased and exceeded 1000 sec, it starts fluctuating between 1000 and 1400 sec. Interestingly, the thrust exceeds the theoretical value of purely electro-magnetic origin, which is given as follows (Ref. 8):

$$F_{em} = \frac{\mu_0 J^2}{4\pi} \left[\ln \frac{Ra}{Rc} + \alpha \right], \quad \alpha = 0 \sim 3/4, \tag{43}$$
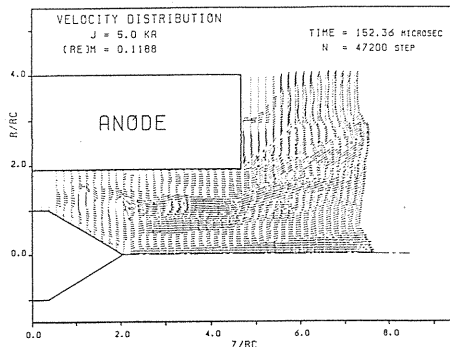
where α is a parameter related with thruster geometry. The thrust maximum and minimum in Fig. 13 occur at $\alpha=0$ and $\alpha=3/4$ in Eq. (43). The fluctuation of the thrust between 3 and 5 N is conceivably caused by the observed oscillation of the flow.

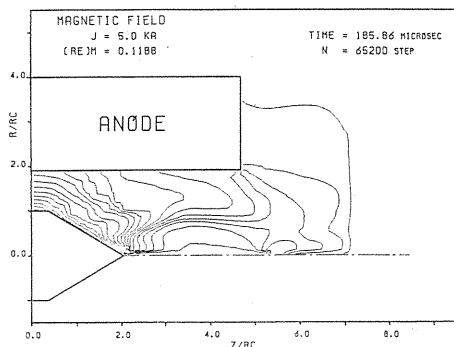The voltage between the cathode and anode is defined as

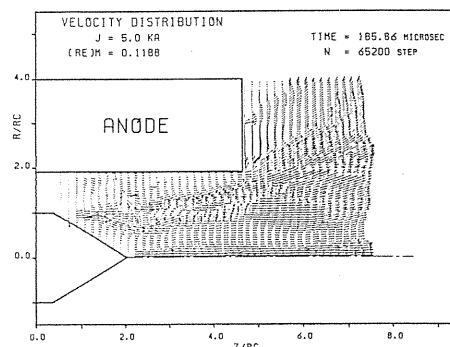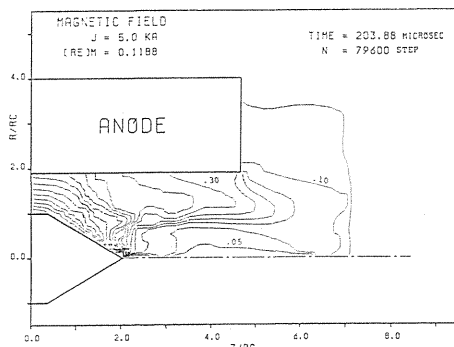$$V = \frac{P_J}{J} = \left[\int_V \boldsymbol{j} \cdot \boldsymbol{E} dV \right] / J, \tag{44}$$
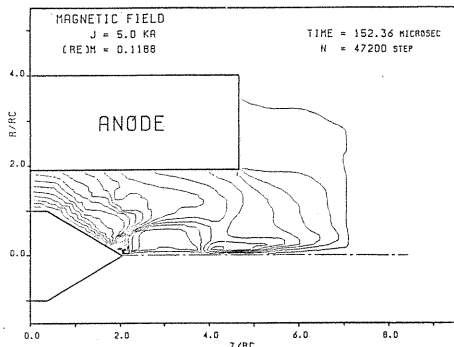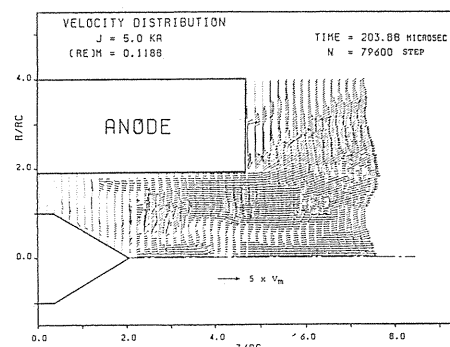
Fig. 10. Temporal behaviors of magnetic flux intensity taking account of Hall effect ($R_m=0.1188$).

Fig. 11. Temporal behaviors of velocity vector taking account of Hall effect ($R_m=0.1188$).

where P_j is the electric power input dissipated by Joule heating. The voltage defined above does not reflect a spatially continuous profile but a discontinuous potential difference. As no electrode sheath is considered in the present analysis, in addition, no electrode voltage fall comes into play, either. The calculated potential difference is about 10 V, consisting of the voltage due to the kinetic energy of the plasma gas and the voltage caused by the thermal energy that is not
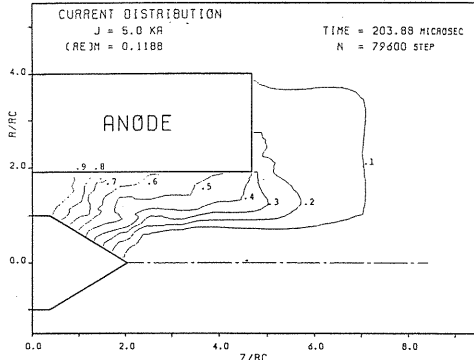
12 (a)
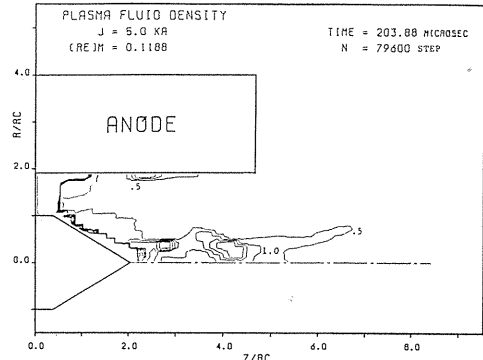
12 (b)
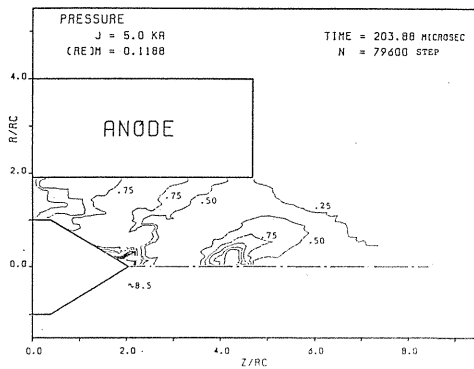
12 (c)

$(R_m = 0.1188)$.

Fig. 12. (a) Current distribution contours,
       (b) plasma density contours and
       (c) pressure contours with Hall effect

converted into the kinetic energy. Since it is reported that the potential differences measured by existing experiments is about 40 V (Ref. 9), the remaining 30 V would be attributed to the electrode fall and other loss falls. The calculated results show a good agreement with experimental data (Refs. 9~10), implicating the convenience of the MHD analysis to predict macroscopic values.

One of the most important aspects in the present type of computation is the computing speed to acquire a solution on a flow field. Although the code is vectorized well enough for the FACOM VP-200, it took 21.6 μsec per time step per grid point for purely gasdynamic and 52.2 μsec for magneto-hydrodynamic calculations: The MHD code runs 2.4 times slower than the gasdynamic code.
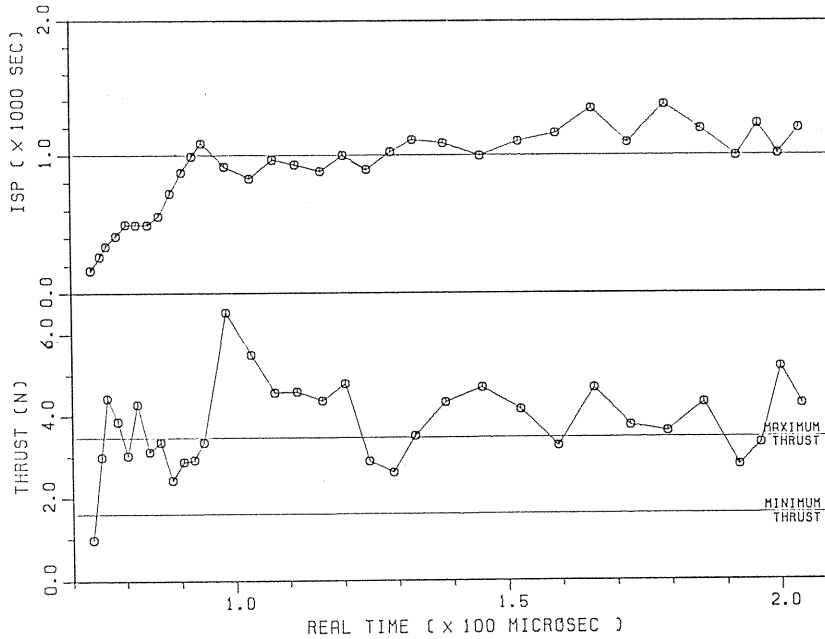
Fig. 13. Isp and thrust versus real time.

5. Conclutions

(1)   Various performances of an MPD thruster (Isp, thrust etc.) can be predicted by the analysis using the MHD equations and one-fluid model.

(2)   The SOSA technique is effective to advance the time by a meaningful amount without causing numerical instabilities. The fluid mechanical analysis for an arbitrary-geometry MPD thruster can be performed using this code, while the computing time is still too long (5-hour CPU time), even if the SOSA technique is employed. In order to eliminate this difficulty, an analysis using an implicit method is in progress assuming steady flows.

References

1) T. Ao and T. Fujiwara; Numerical and Experimental Study of an MPD Thruster, JASS/AIAA/DGLR, 17th International Electric Propulsion Conference, Tokyo, 84-08, 1984.

2) T. Ao and T. Fujiwara; Numerical Analysis of an MPD Thruster Using One-Fluid Model, Report on Theoretical and Experimental Molecular-gas Dynamics (in Japanese), Nagoya University, School of Engineering, pp. 109-125, 1985.

3) H. Yamada, T. Ao and T. Fujiwara; Two-Dimensional Analysis of a Flow in an MPD Thruster, Proceedings of the Symposium on Mechanics for Space Flight, pp. 67-76, ISAS, 1984.

4) L. Spitzer Jr.; Physics of Fully Ionized Gases (2nd Edition), pp. 136–143, Interscience Publisher, 1962.

5) F. Takayama, S. Taki, T. Fujiwara et al.; Numerical Analysis of Mixing and Ignition of Hydrogen in Hot Gas, International Symposium on Computational Fluid Dynamics-Tokyo, pp. 496–506, 1985.

6) K. Goto; Plasma Physics (in Japanese), pp. 121–127, Kyorits Publishing Inc, 1967.

7) W. G. Vincenti and C. H. Kruger Jr.; Introduction to Physical Gas Dynamics, pp. 12–14, John Wiley and Sons, 1965.

8) R. G. Jahn; Physics of Electric Propulsion, pp. 240–246, McGraw-Hill, 1968.

9) H. Tahara, Y. Kagaya and T. Yoshikawa; Arc Structure in a Quasi-Steady MPD Thruster, J. of JSASS, Vol. 33, 1985.

10) T. Fujiwara, T. Ao and M. Aoki; Parametric Study of MPD Thrusters in a Low-Density Wind Tunnel, AIAA paper, 86-0135.